



## A Process for Radiometric Correction of UAV Image Blocks

EIJA HONKAVAARA, TEEMU HAKALA, LAURI MARKELIN, TOMI ROSNELL, Masala, HEIKKI SAARI & JUSSI MÄKYNEN, Espoo, Finland

**Keywords:** Reflectance, radiometry, geometry, calibration, UAV, hyperspectral

**Summary:** The objective of this investigation is to develop and test a radiometric correction process for UAV image blocks. The phases of the process include the laboratory calibration of the sensor and the radiometric correction of the campaign image data. This investigation focuses on developing a process for radiometric correction of the image data collected during a remote sensing campaign. First of all, the orientations for the images are determined using the self-calibrating bundle block adjustment method and an accurate DSM is generated by automatic image matching. The varying radiometric level of images due to changes in illumination and the instability of the sensor are eliminated using a relative radiometric block adjustment technique. Optional reflectance reference observations can be used to adjust the data to absolute reflectance units. The process was demonstrated and evaluated by using two UAV imaging systems: a consumer camera-based system and a novel Fabry-Perot interferometer-based next generation lightweight hyperspectral imaging system. The method improved the homogeneity of the data, but some drift also appeared in the parameters. The first experiment provided 0.003–0.008 reflectance errors in the areas close to the radiometric control points (mostly on the level of 5 % of the reflectance value). The presented approach provides a general framework for rigorous radiometric correction of UAV image blocks, and the novel technology provides many possibilities for the further development of the method. Our results also show that hyperspectral stereophotogrammetry is now possible with UAV imaging sensors weighing less than 500 g.

**Zusammenfassung:** *Verfahren zur radiometrischen Korrektur von UAV Bildblöcken.* Das Thema der vorgestellten Untersuchung ist die Entwicklung und der Test eines Korrekturverfahrens für die Radiometrie eines Bildblocks, der mit kleinen unbemannten Flugzeugen aufgenommen wurde (UAVs = Unmanned Aerial Vehicles). Das Verfahren umfasst die Laborkalibrierung der Kamera und die radiometrische Korrektur der bei der Befliegung aufgenommenen Bilddaten, und ist vor allem auf fernerkundliche Anwendungen ausgerichtet. Im ersten Schritt werden die Bilder über eine Aerialtriangulation verknüpft, wobei die Parameter der inneren Orientierung mitgeschätzt werden (Selbstkalibrierung). Dann folgt die Ableitung eines digitalen Oberflächenmodells. Die radiometrischen Unterschiede zwischen den einzelnen Bildern bedingt durch Beleuchtungsunterschiede und Instabilität des Sensors werden durch ein neues Verfahren zur relativen radiometrischen Blockausgleichung entfernt. Optional können Referenzreflektanzen eingeführt werden, um auf diese Weise den aufgenommenen Daten absolute Reflektanzwerte zuordnen zu können.

Das Verfahren wurde mit Bilddaten zweier auf UAVs betriebener Systeme erprobt. Es handelte sich einerseits um eine Consumer-Kamera und andererseits um eine neue Hyperspektralkamera von Fabry-Perot, die sich durch geringes Gewicht und die Nutzung der Interferometrie auszeichnet. Die Anwendung unseres Verfahrens ließ zwar homogenere Bilddaten entstehen. Gewisse Drafteffekte blieben aber bestehen. Die ersten Untersuchungen zeigten einen RMS-Fehler von 0.003–0.008 der Reflektanzeinheit im Bereich der radiometrischen Passpunkte, meistens in der Größenordnung von 5 % der Reflektanzwerte. Das vorgestellte Verfahren bietet einen Rahmen für eine durchgreifende radiometrische Ausgleichung von Bilddaten, die von UAV-Plattformen aufgenommen werden. Neue Technologien, z. B. der Sensoren, lassen viele weitere Entwicklungen erwarten. Unsere Ergebnisse zeigen, dass hyperspektrale Stereophotogrammetrie von UAVs heute möglich ist, wenn die Sensoren leichter als 500 g sind.

## 1 Introduction

Low-cost and low-weight UAV imaging systems offer great potential for local area remote sensing applications, such as applications for agriculture, forestry, the mining industry and hydrology, as well as for scientific research. To obtain a good reconstruction of the object, images are collected in a block structure with large forward and side overlaps. The multiple observations per image point are of great importance in order to improve the reliability of the data processing and interpretation (LEBERL et al. 2010). Multiple image overlaps are widely used in the geometric processing of images, including the bundle block adjustment methods and surface reconstruction, but there are not yet well-established processes for utilizing the multiple overlaps in radiometric processing for UAV applications.

The idea of radiometric block adjustment is not new. A rigorous method for combining geometric and radiometric object reconstruction, called the global object reconstruction method, was already presented by EBNER & HEIPKE (1988) several decades ago. Unfortunately, the method turned out to be computationally laborious, and in practical applications the geometry and radiometry are processed separately.

Recently, approaches have been established for the radiometric block adjustment and reflectance image generation of image block data collected by stable, large-format digital photogrammetric cameras (CHANDELIER & MARTINOTY 2008, COLLINGS et al. 2011, LÓPEZ et al. 2011). For photogrammetric images, approaches that are based on the radiative transfer theory and that do not account for the overlaps in airborne image blocks have also been developed (BEISL et al. 2008, RICHTER & SCHLÄPFER 2002). In UAV remote sensing applications, empirical line-based approaches are typically used (BERNI et al. 2009), or then simple balancing approaches are used (ZHOU 2009); the analysis is carried out using the central areas of the images. HAKALA et al. (2010) developed a UAV-based method for accurate measurement of the reflectance anisotropy of surfaces, but this method required reflectance reference targets in each image, which is not appropriate in many practical operational re-

mote sensing campaigns; also, other methods for the anisotropy measurements are currently being developed (GRENZDÖRFFER & NIEMEYER 2011).

The radiometric correction is one step in the UAV remote sensing process. The central phases of the image production process include the laboratory calibration of the sensor, data collection, orientation of the images, digital surface model (DSM) generation, radiometric correction and the calculation of the final end products, such as radiometrically corrected images and orthophoto mosaics. The corrected images are utilized in the remote sensing applications.

The objectives of this investigation are to develop a method for radiometric correction and reflectance image generation for UAV imaging that utilizes multiple overlaps in the image block and to demonstrate its use with novel imaging systems. In section 2, the theoretical background of the radiometric correction method is described. In section 3, we describe the set-up for the empirical investigation; we give the results in section 4 and discuss our findings in section 5.

## 2 Novel Radiometric Correction Method

### 2.1 Theoretical Background

In passive UAV imaging, the elementary components of radiance entering the sensor ( $L_{at\_sensor}$ ) are the radiance components from the object of interest, mainly the surface-reflected solar radiance ( $L_s$ ), skylight ( $L_{sky}$ ), background radiance ( $L_{bg}$ ) and the radiance reflected first by the background objects and then by the atmosphere ( $L_{bg\_multi}$ ); the adjacency effect ( $L_{adj}$ ) and atmospheric path radiance ( $L_{atm}$ ) are radiance components that do not carry any information about the object of interest (SCHOTT 2007):

$$L_{at\_sensor} = L_s + L_{sky} + L_{bg} + L_{bg\_multi} + L_{adj} + L_{atm} \quad (1)$$

The contributions of different radiation components in (1) are dependent on the flying height, the atmospheric state, the reflectance

properties of the object of interest and the reflectivity of the surrounding objects; more details can be found in VON SCHÖNERMARK et al. (2004) and SCHOTT (2007).

In this investigation we collected the data in direct sunshine in a flat and open area, so the surface-reflected direct solar radiance is the dominating component:

$$L_s(\lambda, \theta_i, \varphi_i, \theta_r, \varphi_r) = \rho(\lambda, \theta_i, \varphi_i, \theta_r, \varphi_r) \tau_s(\lambda) E_\lambda^0 \cos \theta / \pi \quad (2)$$

where  $\tau_s$  and  $\tau_r$  are the atmospheric transmittance in the solar path and in the path from object to sensor, respectively,  $E_\lambda^0$  is the spectral irradiance on top of the atmosphere and  $\theta$  is the solar incidence angle on a surface ( $\cos \theta$  is given by the vector dot product of the unit vector pointing towards the Sun and the unit vector normal to the surface).  $\theta_i$  and  $\theta_r$  are the illumination and reflected light (observation) zenith angles and  $\varphi_i$  and  $\varphi_r$  are the azimuth angles, respectively.  $\rho(\lambda, \theta_i, \varphi_i, \theta_r, \varphi_r)$  is the bi-directional reflectance distribution function (BRDF) (VON SCHÖNERMARK et al. 2004).

The sensor properties define how the incoming radiation is measured. The digital grey value ( $DN$ ) of a given pixel, after applying dark pixel subtraction and correcting sensor-related radiometric non-uniformities, can be given as follows:

$$DN = GA_d \Omega \tau \int_0^\infty L_{at-sensor}(\lambda) S(\lambda) d\lambda \quad (3)$$

where  $G$  is the system gain,  $A_d$  is the area of the detector,  $\Omega$  is the aperture,  $\tau$  is the integration or exposure time,  $S(\lambda)$  is the system-level spectral response and  $\lambda$  is the wavelength. Depending on the sensor, the  $DN$  value can be controlled by the exposure time, by the aperture and exposure time or by the aperture, by the exposure time and by the ISO setting (ROSNELL et al. 2011). In the following discussion, it is assumed that band-averaged values are being used.

The equation for the reflectance in sun-illuminated conditions with contributions from the path radiance is

$$\rho(\theta_i, \varphi_i, \theta_r, \varphi_r) = (\pi(c_0 + c_1 DN) - L_{atm}) / (\tau_s \tau_v E^0 \cos \theta) \quad (4)$$

where  $c_0$  and  $c_1$  are the absolute radiometric calibration parameters of the sensor when relating the  $DN$ s to  $L_{at-sensor}$ . The reflectance can be solved by physically or empirically based methods (HONKAARA et al. 2009). In low-altitude applications, a linear approximation (empirical line method) is a feasible approach for the reflectance product generation (SCHOWENGERDT 2007), and this is the basis for the development of the method in this investigation:

$$\rho(\theta_i, \varphi_i, \theta_r, \varphi_r) = c'_0 DN + c'_1 \quad (5)$$

where  $c'_0$  and  $c'_1$  are modified calibration coefficients, which are dependent on illumination, the atmosphere and sensor-related factors ((1) and (4)).

## 2.2 A Process for UAV Image Block Radiometric Correction

The empirical model for the conversion of object reflectance to  $DN$  is

$$DN_j = a_{abs} R_j(\theta_i, \varphi_i, \theta_r, \varphi_r) + b_{abs} \quad (6)$$

where  $R_j(\theta_i, \varphi_i, \theta_r, \varphi_r)$  is the bi-directional reflectance factor (BRF) of the object  $j$  and  $a_{abs}$  and  $b_{abs}$  are the parameters of the empirical line model (a reflectance factor is used because it is a measurable quantity (SHAEPMAN-STRUB et al. 2006)).

The  $DN$  value of the same point is different in different overlapping images. In an image block, this is partially caused by the anisotropic characteristic of object reflectance, which is the physical property of the object. Other important factors causing differences include the changes in illumination conditions and the inaccuracy of the exposure of the sensor and other sensor inaccuracies. While the anisotropy of the reflectance is modelled by the BRDF, the relative differences in the overlapping images must be estimated. In this study we used a linear model to model these differences; the extended model for image  $i$  and object  $j$  is

$$DN_{ij} = a_{rel,i}(a_{abs} R_j(\theta_i, \varphi_i, \theta_r, \varphi_r) + b_{abs}) + b_{rel,i} \\ = a_{rel,i} a_{abs} R_j(\theta_i, \varphi_i, \theta_r, \varphi_r) + a_{rel,i} b_{abs} + b_{rel,i} \quad (7)$$

The corresponding observation equation for  $DN$  of object  $j$  in image  $i$ , with a correction  $v_{ij}$ , is

$$v_{ij} = a_{rel\_i} a_{abs} R_j(\theta_i, \varphi_i, \theta_r, \varphi_r) + a_{rel\_i} b_{abs} + b_{rel\_i} - DN_{ij} \quad (8)$$

The observation equation for the radiometric control point with a reflectance observation,  $R_{obs\_j}(\theta_i, \varphi_i, \theta_r, \varphi_r)$  and a correction  $v_j$ , is

$$v_j = R_j(\theta_i, \varphi_i, \theta_r, \varphi_r) - R_{obs\_j}(\theta_i, \varphi_i, \theta_r, \varphi_r) \quad (9)$$

For one of the images, the relative parameters are  $a_{rel\_1} = 1$ ,  $b_{rel\_1} = 0$ , and the other relative parameters are relative to these parameters. Various parameterizations can be used: 1) a full linear model for absolute and relative correction, 2) a linear model for absolute correction and offset for the relative correction, 3) only relative parameters and 4) only absolute parameters. Furthermore, it is possible to estimate the radiometric object model (BRDF).

The radiometric correction process is as follows. A network of radiometric tie points is generated in the campaign area in the object coordinate system. Accurate image orientation information and DSM are needed in order to determine the  $DN$  observations. Observation equations ((8) and (9)) are generated for each image  $DN$  observation and object reflectance observation. The result is an over-determined adjustment task, which can be solved using the least squares method.

The model presented here assumes that the  $DN$ s will be corrected for sensor defects based on calibration information. Central parameters that need to be determined in the laboratory calibration include the corrections for the

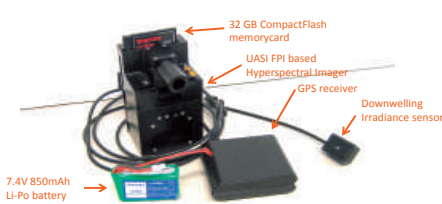
lens falloff and CCD detector non-uniformity as well as the spectral response (SCHOWENGERDT 2007, SCHOTT 2007).

### 3 Empirical Testing

#### 3.1 Imaging Systems

The Microdrones MD4-1000 quadcopter UAV was used as the platform, allowing for a maximum payload of 1000 g. The imaging sensors included a hyperspectral prototype sensor developed by the VTT Technical Research Centre of Finland (MÄKYNEN et al. 2011, SAARI et al. 2011) and a Panasonic Lumix GF1 customer micro four-thirds camera (Fig. 1). Both systems are capable of collecting stereoscopic image data.

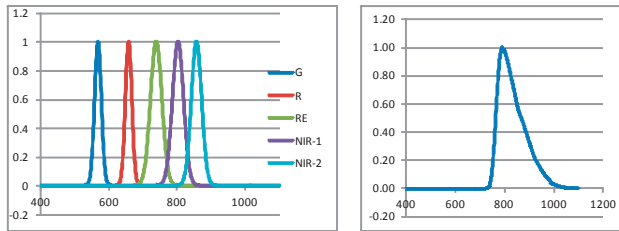
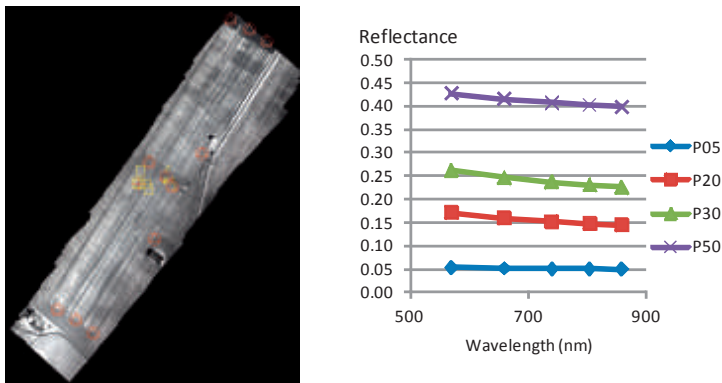
The Fabry-Perot interferometer (FPI) based hyperspectral imaging sensor represents the next generation in imaging technology (Unmanned Aerial System Innovations, UASI) (MÄKYNEN et al. 2011, SAARI et al. 2011). When the FPI is placed in front of the sensor, the sensitivity of each pixel is a function of the interferometer air gap. By changing the air gap, it is possible to acquire a new set of wavelengths for each image. With a sequence of images captured with different air gaps of the FPI, it is possible to reconstruct the spectrum for each pixel in the image. In this mode, up to 54 raw images can be saved to buffer memory in one image burst. The camera weighs only 450 g. The prototype uses the 5 Mpix RGB CMOS image sensor MT9P031 from APTINA (2011), and the  $4 \times 4$  binned Video Graphics Array (VGA) was used in the flight campaign. Details about the camera are given in Tab. 1 and Fig. 2.



**Fig. 1:** Left: VTT hyperspectral camera UASI (SAARI et al. 2011). Right: Panasonic Lumix GF1 cameras.

**Tab. 1:** Parameters of sensors. F: focal length; FOV f, FOV cf: field of view in flight and cross flight directions.

Sensor	F (mm)	Pixel ( $\mu\text{m}$ )	Columns	Rows	FOV f ( $^\circ$ )	FOV cf ( $^\circ$ )	Weight (g)
UASI	0.0093	8.8	640	480	26	36	450
GF1	0.020	4.5	4016	3016	37	48	448

**Fig. 2:** Left: selected channels of hyperspectral data (central band width, full width of half maximum FWHM): G: 568.553 nm, 23.287 nm; R: 658.459 nm, 22.324 nm; Red edge (RE): 739.082 nm, 29.724 nm; NIR-1: 802.868 nm, 38.38 nm; NIR-2: 857.029 nm, 35.601 nm. Right: spectral response of the GF1.**Fig. 3:** Left: overview of the block: ground control points (red triangles), right: spectra of the reflectance targets for the five selected UASI channels (Fig. 2).

The Panasonic Lumix GF1 camera (LUMIX 2011) has been modified so that it works as an NIR camera (see details in Tab. 1, Fig. 2). In this study, only the pixels stored in the red channel were used.

### 3.2 Flight Campaigns

The image blocks collected at the MTT Agrifood Research Finland agricultural test site (N 60° 25' 21", E 24° 22' 28") on 6 July, 2011 were used to test the radiometric correction method (Fig. 3). Four reflectance reference

tarps (nominal reflectance: 0.05, 0.2, 0.3, 0.5), a Siemens star and 11 ground control points were used as reference targets. The reflectance of the reference tarps was measured using the ASD Field Spec Pro FR spectroradiometer and the measurements were normalized to a calibrated, white, 30 cm by 30 cm Spectralon reference standard from Labsphere. In this study, a single image strip from both sensors was used; the forward overlaps were 81 % and 91 % for UASI and GF1, respectively. The length of the area was approximately 500 m and the width of the image strip was approximately 80 m with UASI and 120 m with GF1.

**Tab. 2:** Details on the data collection (S.E: solar elevation, S.Az: solar azimuth)

Sensor	Time	f-stop	T (s)	GSD (cm)	Forward Overlap (%)	Images	S.E. (°)	S.Az. (°)
UASI	9:25	<7.0	1/300	13	81	42	45	132
GF1	11:06	5.0	1/2000	3	91	57	52	166

In the campaigns, the sensors were not operated simultaneously because a suitable camera mount was not available. The weather conditions during the campaign were fine, with almost a cloud-free sky and moderate wind (Tab. 2).

### 3.3 Radiometric Calibration in Laboratory

The spectral and lens fall-off calibration of the UASI were carried out at the VTT's calibration facility. The spectral calibration was carried out using a Quartz halogen lamp, a monochromator (Bentham TMc300) and a beam homogenizer and diffuser module to provide an evenly distributed narrow bandwidth light, which was projected into the hyperspectral imager optics. The calibration of the spectral radiance was performed with the aid of a United Detector QED-200 absolute radiometer for the wavelength range of 350–1050 nm using 1 nm steps and a FWHM resolution of 1 nm. After this, the UASI hyperspectral imager was attached to the setup and its signal for each wavelength was recorded at 280 FPI air gap values in the range of 100–1500 nm at 5 nm intervals. The calibration measurements were used to calculate the calibration coefficient matrix. The spectral photon flux entering the pixels of the hyperspectral imager at a fixed FPI air gap can be calculated by multiplying the Red (R), Green (G) and Blue (B) pixel signals by the calibration coefficient matrix for the whole image (MÄKYNEN et al. 2011, SAARINEN et al. 2011). The lens falloff calibration of the UASI was performed using an integrating sphere and a Quartz halogen lamp to provide a uniform, wide-band radiance. The lens fall-off factor was calculated from an average of 10 raw images, from which dark images at the same exposure time were subtracted.

The radiometric camera calibration of the GF1 was carried out at the Finnish Geodetic Institute's (FGI) experimental calibration facility. The spectral calibration was carried out using a stabilized 50 W quartz tungsten halogen lamp (Thermo Oriol 66881), an Oriol Cornerstone 74125 monochromator and a diffuser. The output of the monochromator was first measured using an ASD Field Spec Pro FR spectroradiometer, which had an FWHM of 3 nm at a range of 350–1000 nm. The GF1 was then used to capture a set of images at 10 nm intervals at a range of 350–1000 nm, and the spectral response was calculated from this dataset. The lens falloff correction was determined by photographing white isotropic reference (PTFE plane of the size 1 m x 1 m in diffuse illumination conditions in cloudy weather) and fitting a  $\cos^n$  function (SCHOTT 2007) to 8 images; a value of 5.6 was obtained for n.

### 3.4 Data Processing

The data processing began by carrying out the image correction using correction factors determined by the laboratory calibration. The further processing was carried out in a photogrammetric environment consisting of the BAE Systems SOCET SET photogrammetric workstation (DEVENECIA et al. 2007, WALKER 2007) and in-house developed components.

The orientation determination of the GF1 images was relatively efficient. A small amount of manual interaction was necessary because the GNSS/IMU system did not provide accurate enough a priori orientation information for the SOCET SET automatic tie point determination method. Orientation determination was carried out in two phases: in the first iteration, a small number of interactively measured tie points were used to

provide satisfying approximate orientations, and in the second iteration 121 automatically measured tie points per image were computed using the SOCET SET. In self-calibrating bundle block adjustments, the principal point, radial distortions and tangential distortions were estimated. The Next Generation Automated Terrain Extraction software (NGATE) (DEVENECIA et al. 2007) was used to determine 3D point clouds. The point cloud was created with a 10 cm point interval using the default NGATE strategy (ngate.strategy with a correlation window size of  $5 \times 5$  pixels). The planimetric and vertical accuracy of the georeferencing (image mosaics, point clouds and 3D point determination) was estimated to be better than 0.2 m. Examples of a GF1 image and derived point cloud are shown in Fig. 4.

The orientation processing of the UASI images followed the same principles as the processing of the GF1 images. The challenge in

processing them was that the individual channels of the spectral data cube were collected within a short period of time (in this set up, approximately in 1 s). Due to the platform movements, the individual channels do not overlap accurately, as is demonstrated in Fig. 5. In this study, 5 channels (Fig. 2) were selected from a hyperspectral data cube with 50 channels, and each channel was oriented separately. A further complication was that the adjustment appeared to be quite unstable; thus, only the first-order radial distortion parameter was used to model image distortions. Approximately 20 additional GCPs were extracted using the GF1 image block to aid the orientation. It was estimated that the accuracy of the georeferencing was better than 0.5 m for all of the coordinate components. The method for the orientation processing will be improved in the future.

The radiometric block adjustments were carried out using the methodology described

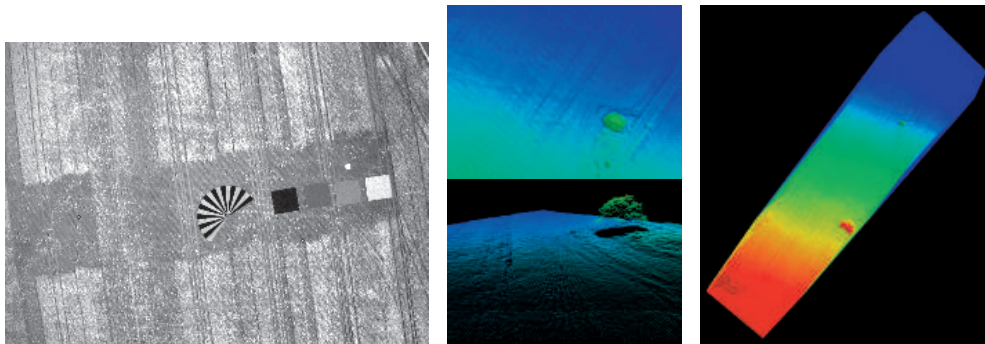


**Fig. 4:** Left: GF1 image, centre and right: Different views of the point cloud generated from GF1 images by automated image matching.

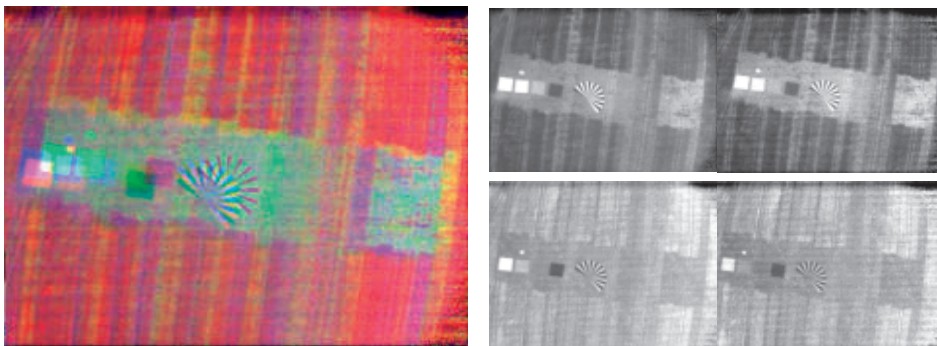


**Fig. 5:** Left: an example of an UASI image with the channels NIR-2, G and R, top-right: UASI-channels G and R, bottom right: UASI-channels red edge and NIR-2.

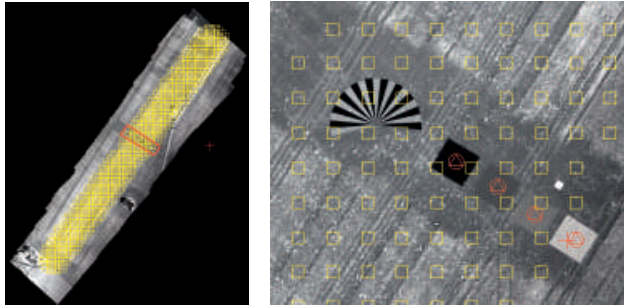


**Fig. 6:** Radiometric tie points (yellow) and control points (red) in a GF1 image strip.

in section 2.2. In this investigation, the method was used to eliminate the radiometric differences of overlapping images, which could be due to sensor inaccuracy or illumination differences, and for reflectance image generation. A grid of radiometric tie points was created with a 5 m point interval (Fig. 6), and the image coordinates of the tie points were calculated using the orientations and the DSM. *DN* observations were taken from all images having a view angle to the object point of less than  $10^\circ$ ; it was assumed that with small view angles, the BRDF effects were limited so that the BRDF model could be ignored. The average of *DN*s in a small image window was used as the *DN* observation (UASI:  $5 \times 5$  pixels, GF1:  $30 \times 30$  pixels). Different parameterizations were tested. Depending on the illumination situation, different reflectance quantities may be obtained (SCHAEPMAN-STRUB et al. 2006). In this study, with direct sunshine, the approach provides BRFs.

### 3.5 Performance Assessment

The quality of the adjusted model parameters was evaluated by using the standard deviation estimates provided by the least squares method.

The variation coefficients (standard deviation divided by the average value) in each tie point were used to evaluate the homogeneity of the data before ( $VCF_{original\ image}$ ) and after the correction ( $VCF_{corrected\ image}$ ). The homogenization factor (*HF*) is (LÓPEZ et al. 2011) as follows:

$$HF (\%) = \frac{VCF_{original\ image} - VCF_{corrected\ image}}{VCF_{original\ image}} \times 100 \quad (10)$$

The overall *HF* was calculated as an average of the *HF*s for all radiometric tie points.

The differences in the radiometric control points were used to evaluate the accuracy of the reflectance images. The root-mean-square error (RMSE) was calculated for all of the control points and images with the targets.

## 4 Results

### 4.1 Radiometric Block Adjustments

We carried out radiometric block adjustments with different combinations of relative and absolute parameters (8). The tested models were 1) relative offset ( $b_{rel\_1} \dots b_{rel\_n}$ ), 2) relative linear model ( $a_{rel\_1} \dots a_{rel\_n}, b_{rel\_1} \dots b_{rel\_n}$ ) and 3) absolute linear model and relative offset ( $a_{abs}, b_{abs}, b_{rel\_1} \dots b_{rel\_n}$ ).

Fig. 7a shows the impact of correction on the average variation coefficient of the radiometric tie points. The homogenization factors (10) were with both sensors approximately 20–50% with both relative correction scenarios, which means that grey value differences decreased with relative radiometric correction; the homogeneity was similar with single- and two-parameter relative correction models (models 1 and 2). The homogenization factors deteriorated in the cases with absolute radiometric correction (model 3). An example of a successful elimination of the radiometric differences of images in an image mosaic is shown in Fig. 7b.

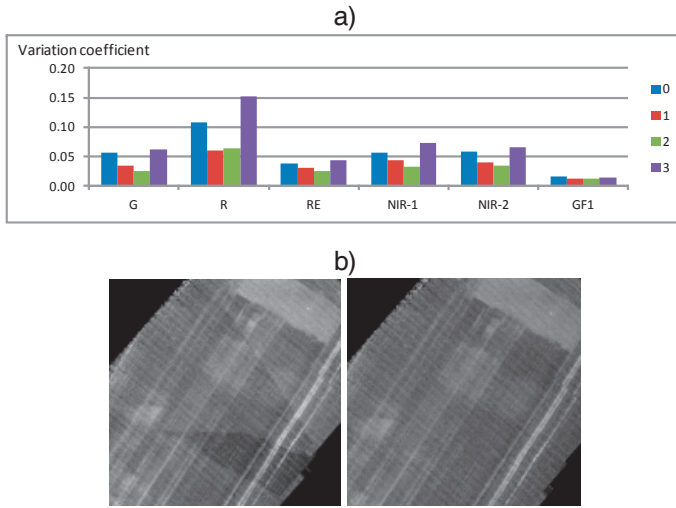


**Fig. 7:** a) Average variation coefficients of radiometric tie points for different channels with different models. 0: original images; 1: relative offset ( $b_{rel,1} \dots b_{rel,n}$ ); 2: relative linear model ( $a_{rel,1} \dots a_{rel,n}$ ,  $b_{rel,1} \dots b_{rel,n}$ ); 3: absolute linear model and relative offset ( $a_{abs}$ ,  $b_{abs}$ ,  $b_{rel,1} \dots b_{rel,n}$ ). b) An example of the successful relative radiometric correction in red channel.

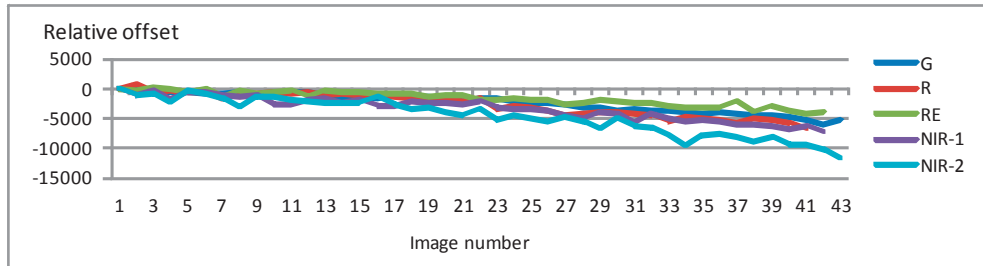


**Fig. 8:** The relative offset parameter ( $b_{rel,1} \dots b_{rel,n}$ ) of different images.

The relative offset parameter of different images is shown in Fig. 8. The parameters are related to the topmost image in the image strip ( $b_{rel,1} = 0$ ). A drift appeared in the offset parameters. The absolute parameters correlated strongly with the reflectance unknowns, which indicated that the solution was not quite controlled. Some constraints would be needed to eliminate the drift and correlations.

#### 4.2 Accuracy of Reflectance Images

Examples of image mosaics produced from lens-fall-off corrected images and reflectance images are shown in Fig. 9. The brightening of the mosaics towards the West-North direction is due to the BRDF effects; the sunshine

was from the South-East direction, which is about perpendicular to the flight direction. The darkening of the UASI mosaic towards the North-East direction is most likely due to problems with the correction parameters and the soil properties.

We evaluated the accuracy of the reflectance images using the reflectance tarps. Two cases were evaluated: 1) for the block adjustment, we used absolute and relative parameters ( $a_{abs}$ ,  $b_{abs}$ ,  $b_{rel,1} \dots b_{rel,i}$ ), and 2) we calculated the empirical line parameters using one image and used the parameters to correct the other images (3 images with UASI, 4 images with GF1). Reflectance differences (RMSE-value) in the reflectance reference targets are shown in Fig. 10. The RMSEs were mostly 0.006–0.008 for the reflectance units

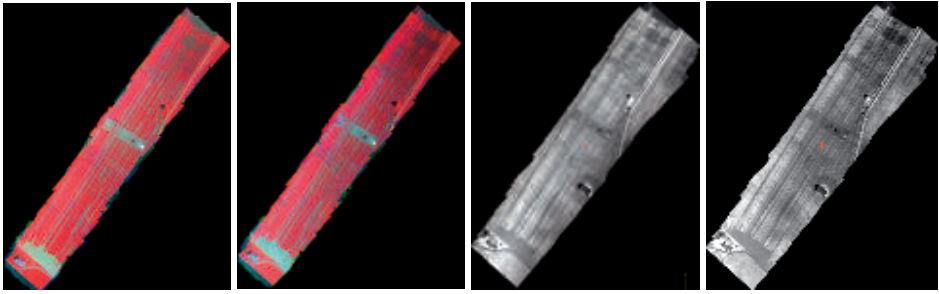


**Fig. 9:** From left to right: Original and reflectance UASI mosaic, original and reflectance GF1 mosaic. (North is up, East is to the right).

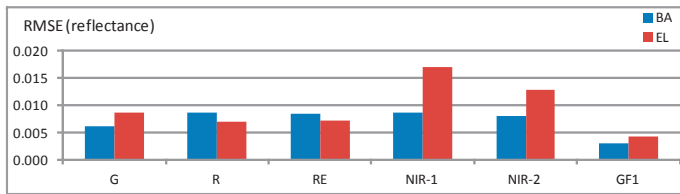


**Fig. 10:** Reflectance error (RMSE) in reflectance images in different channels (BA: radiometric block adjustment, EL: empirical line method).

and 5–7% of the reflectance value. With the empirical line method, larger differences appeared in NIR-1 and NIR-2 channels (large errors in the black target with a nominal reflectance of 0.05). In these channels, the block adjustment provided better accuracy. Reflectance errors were slightly lower in the GF1 images than in the UASI images, which could be the result of several factors: the lower georeferencing accuracy of UASI could cause larger standard deviations; the atmospheric conditions might have been different (a sun-photometer was not used during the campaign); or, higher noise in UASI images (Figs. 4 and 5). According to laboratory testing, the UASI is very stable. This evaluation gives accuracy in the areas close to the reflectance targets. Furthermore, the accuracy assessment is not independent in the case of block adjustment, because the same points were used in the adjustment and in the evaluation; thus, the result mainly validates the processing.

We made the following conclusions. The relative radiometric correction was necessary with the datasets and the offset parameter ( $b_{rel}$ ) was sufficient for the relative correction. For the reflectance image generation the absolute linear model is required ( $a_{abs}$ ,  $b_{abs}$ ). The meth-

od has to be further improved in order to control the drifts and correlations.

### 5 Discussion

We developed a radiometric correction method for UAV image blocks which utilizes multiple overlaps in an image block and demonstrated the use of the method. Images were collected using two different imaging systems: a next-generation hyperspectral imaging system based on Fabry-Perot interferometer and developed by the VTT Technical Research Centre of Finland (MÄKYNEN et al. 2011, SAARI et al. 2011), and a commercial customer camera, both weighing less than 500 g.

The results showed that the method improved the homogeneity of an image block. The method is more economic than a method requiring a reflectance reference target in every image. The solution is computationally efficient because only a limited number of tie points have to be used.

There are several possibilities to improve the performance of the method. An elimination method for the outliers needs to be implemented; some approaches have been presented

in previous literature on the topic (CHANDILIER & MARTINOTY 2008, LÓPEZ et al. 2011). In this study, the object was quite homogeneous, so the outliers were not a serious problem. It is necessary to implement a BRDF model to improve the processing; for example, in order to adjust several image strips together and to provide radiometrically homogeneous image mosaics. Simple linear models were used for the absolute and relative correction; it is possible to use more rigorous models for atmospheric parameters ((1) and (4)). Number of reflectance unknowns could be decreased in order to eliminate the correlations. It is feasible to collect additional observations of the imaging conditions during UAV campaigns (for example, by using a sunphotometer or by using an irradiance sensor to collect observations of downwelling radiance, which is a component of the UASI) and to use them to constrain the method. Furthermore, in the case of hyperspectral sensors, it is possible to estimate some atmospheric parameters using appropriate channels. Using radiometric control points with a better distribution would probably decrease the systematic drift of the correction. It can be concluded that the approach presented here offers a powerful and flexible framework for rigorous and reliable radiometric correction.

We processed only five channels of the 50 channel hyperspectral data cube in order to prove the concept. The conventional photogrammetric workstation SOCET SET was not functional in the orientation determination of the small-format UASI images with large rotational differences and poor approximate orientation values. More efficient georeferencing approach has to be developed. The processing time for the radiometric correction is directly proportional to the number of channels processed.

The radiometric correction of low-altitude UAV images has many advantages in comparison to airborne imaging from a higher altitude using large-format cameras. It is feasible to install reflectance reference targets and irradiance sensors in the campaign area because the operator has to go to the area anyway. Atmospheric disturbances are much lower due to the shorter distances. On the other hand, many well-established radiometric correction methods are not possible in many UAV cam-

paigns, for example when using dark vegetation to provide a dark pixel values for correction methods based on dark pixel subtraction or when using spectral libraries as a reference. One characteristic of UAV campaigns is that they will need to be carried out under variable conditions, which has to be taken into account when developing the correction method.

The prerequisites for the method are accurate image orientations and DSM. The recent results have shown that the novel image matching methods provide sufficiently accurate DSMs for the object surfaces (LEBERL et al. 2010, HIRSCHMÜLLER 2011, ROSNELL et al. 2011), and this is the starting point for developing novel radiometric processing methods. Furthermore, radiometric laboratory calibration is required in order to utilize the image radiometry quantitatively.

## 6 Conclusions

Efficient methods are needed for the radiometric correction of UAV image blocks. In this study, we demonstrated the radiometric block adjustment of UAV image block. The approach is flexible and the novel sensing technology provides many possibilities for improving the method. Our investigation also shows that hyperspectral stereophotogrammetry is now possible with lightweight UAV imaging systems.

## Acknowledgements

The research carried out in this study was funded by the Academy of Finland (Project No. 134181).

## References

- APTINA LTD.: [http://www.aplina.com/products/image\\_sensors/mt9p03li12stc/](http://www.aplina.com/products/image_sensors/mt9p03li12stc/) (13.1.2012).
- BEISL, U., TELAAR, J. & V. SCHÖNERMARK, M., 2008: Atmospheric correction, reflectance calibration and BRDF correction for ADS40 image data. – The International Archives of the Photogrammetry, Remote Sensing and Spatial Information Sciences **37** (B7).
- BERNI, J.A., ZARCO-TEJADA, P.J., SUÁREZ, L. & FERRERES, E., 2009: Thermal and Narrowband Multi-

- spectral Remote Sensing for Vegetation Monitoring from an Unmanned Aerial Vehicle. – *IEEE Transactions on Geosciences and Remote Sensing* **47**: 722–738.
- CHANDELIER, L. & MARTINOTY, G., 2009: Radiometric aerial triangulation for the equalization of digital aerial images and orthoimages. – *Photogrammetric Engineering & Remote Sensing* **75** (2): 193–200.
- COLLINGS, S., CACETTA, P., CAMPBELL, N. & WU, X., 2011: Empirical models for radiometric calibration of digital aerial frame mosaics. – *IEEE Transactions on Geoscience and Remote Sensing* **49** (7): 2573–2588.
- DEVENECIA, K., WALKER, S. & ZHANG, B., 2007: New approaches to generating and processing high resolution elevation data with imagery. – FRITSCH, D. (ed.): *Photogrammetric Week 2007*: 297–308.
- EBNER, H. & HEIPKE, C., 1988: Integration of digital image matching and object surface reconstruction. – *International Archives of Photogrammetry and Remote Sensing* **27** (B11(III)): 534–545.
- GRENZDÖRFFER, G.J. & NIEMEYER, F., 2011: UAV based BRDF-measurements of agricultural surfaces with PFIFFIKUS. – *International Archives of the Photogrammetry, Remote Sensing and Spatial Information Sciences* **38** (1/C22).
- HAKALA, T., SUOMALAINEN, J. & PELTONIEMI, J.I., 2010: Acquisition of Bidirectional Reflectance Factor Dataset Using a Micro Unmanned Aerial Vehicle and a Consumer Camera. – *Remote Sensing* **2** (3): 819–832.
- HIRSCHMÜLLER, H., 2011: Semi-Global matching: motivation, development and applications. – FRITSCH, D. (ed.): *Photogrammetric Week 2011*: 173–184.
- HONKAVAARA, E., ARBIOL, R., MARKELIN, L., MARTINEZ, L., CRAMER, M., BOVET, S., CHANDELIER, L., ILVES, R., KLONUS, S., MARSHALL, P., SCHLÄPFER, D., TABOR, M., THOM, C. & VEJE, N., 2009: Digital airborne photogrammetry – A new tool for quantitative remote sensing? – A state-of-the-art review on radiometric aspects of digital photogrammetric images. – *Remote Sensing* **1** (3): 577–605.
- HUNT, E.R. JR., HIVELEY, W.D., FUJIKAWA, S.J., LINDEN, D.S., DAUGHTRY, C.S.T. & MCCARTY, G.W., 2010: Acquisition of NIR-Green-Blue Digital Photographs from Unmanned Aircraft for Crop Monitoring. – *Remote Sensing* **2**: 290–305.
- LEBERL, F., IRSCHARA, A., POCK, T., MEIXNER, P., GRUBER, M., SCHOLZ, S. & WIECHERT, A., 2010: Point clouds: Lidar versus 3D vision. – *Photogrammetric Engineering & Remote Sensing* **76** (10): 1123–1134.
- LÓPEZ, D.H., GARCÍA, B.F., PIQUERAS, J.G. & AOCÁZAR, G.V., 2011: An approach to the radiometric aerotriangulation of photogrammetric images. – *ISPRS Journal of Photogrammetry and Remote Sensing* **66** (2011): 883–893.
- LUMIX, 2012: Panasonic Lumix GF1. – <http://panasonic.net/avc/lumix/systemcamera/gms/gf1/specifications.html> (13.1.2012).
- MÄKYNEN, J., HOLMLUND, C., SAARI, H., OJALA, K. & ANTILA, T., 2011: Unmanned aerial vehicle (UAV) operated megapixel spectral camera. – *Proc. SPIE* 8186 (B).
- RICHTER, R. & SCHLÄPFER, D., 2002: Geo-atmospheric processing of airborne imaging spectrometry data. Part 2: atmospheric / topographic correction. – *International Journal of Remote Sensing* **23** (13): 2361–2649.
- ROSNELL, T., HONKAVAARA, E. & NURMINEN, K., 2011: On geometric processing of multi-temporal image data collected by light UAV systems. – *International Archives of the Photogrammetry, Remote Sensing and Spatial Information Sciences* **38** (1/C22, A).
- SAARI, H., PELLIKKA, I., PESONEN, L., TUOMINEN, S., HEIKKILÄ, J., HOLMLUND, C., MÄKYNEN, J., OJALA, K. & ANTILA, T., 2011: Unmanned Aerial Vehicle (UAV) operated spectral camera system for forest and agriculture applications. – *Proc. SPIE* 8174.
- SCHAEPMAN-STRUB, G., SCHAEPMAN, M.E., PAINTER, T.H., DANGEL, S. & MARTONCHIK, J.V., 2006: Reflectance quantities in optical remote sensing – definitions and case studies. – *Remote Sensing of Environment* **103**: 27–42.
- SCHOTT, J.R., 2007: *Remote sensing: The image chain approach*. – 2nd ed., 666 p., Oxford University Press.
- SCHOWENGERDT, R.A., 2007: *Remote Sensing, Models and Methods for Image Processing*. – 3rd ed., Academic Press Inc., San Diego, CA, USA.
- SUOMALAINEN, J., HAKALA, T., PELTONIEMI, J. & PUTTONEN, E., 2009: Polarised multiangular reflectance measurements using the Finnish geodetic institute field goniospectrometer. – *Sensors* **9** (5): 3891–3907.
- WALKER, S., 2007: New features in SOCET SET®. – FRITSCH, D. (ed.): *Photogrammetric Week 2007*: 35–40.
- VON SCHÖNERMARK, M., GEIGER, B. & RÖSER, H.P., 2004: *Reflection properties of vegetation and soil: with a BRDF data base*. – 1st ed., 352 p., Wissenschaft und Technik Verlag, Berlin, Germany.
- ZHOU, G., 2009: Near Real-Time Orthorectification and mosaic of small UAV video flow for time-critical event response. – *IEEE Trans. on Geoscience and Remote Sensing* **47**: 739–747.

Addresses of the Authors:

Dr. EIJA HONKAVAARA, TEEMU HAKALA, LAURI MARKELIN & TOMI ROSNELL, Finnish Geodetic Institute, Geodeetinrinne 2, 02430 Masala, Finland, Tel.: +358-40-192-0835 (Honkavaara), +358-9-295550 (others), Fax: +358-9-29555200, e-mail: first name.last name@fgi.fi

Dr. HEIKKI SAARI & JUSSI MÄKYNEN, VTT Technical Research Centre of Finland, P.O. Box 1000, 02044 VTT, Finland, Tel.: +358-40-5891254, +358-20-722 111, Fax: +358-20-7227012, e-mail: heikki.saari@vtt.fi, jussi.makynen@vtt.fi

Manuskript eingereicht: November 2011  
Angenommen: Januar 2012